Lidar and Triple-Wavelength Doppler Radar Measurements of the Melting Layer: A Revised Model for Dark and Bright Band Phenomena

Kenneth Sassen[1], James R. Campbell[2], Pavlos Kollias[3], Matthew Shupe[4], Christopher Williams[5], and Jiang Zhu[1]

1. Geophysical Institute, University of Alaska Fairbanks, Fairbanks, AK
2. Science Systems and Applications, Inc., Greenbelt, MD
3. Rosenstiel School of Marine and Atmospheric Science, University of Miami, FL
4. NOAA Environmental Technology Laboratory, Boulder, CO
5. University of Colorado Cooperative Institute for Research in Environmental Sciences and NOAA Aeronomy Labatory, Boulder, CO

Abstract. During a recent field campaign in southern Florida, rain showers were probed by a 0.523 μm lidar and three (0.32-, 0.86-, and 10.6-cm) Doppler radars. The full range of backscattering phenomena was observed in the melting region, including the lidar and radar dark and bright bands. In contrast to the 10.6-cm radar data, only intermittent evidence is found at 0.86 cm for the radar bright band, and no clear examples are seen at 0.32 cm. Analysis reveals that the 0.86-cm radar dark band is due to non-Rayleigh scattering effects in large water-coated snowflakes. The lidar dark band exclusively involves mixed-phase particles and is centered where severely melted snowflakes collapse into raindrops, where spherical particle backscattering mechanisms first come into prominence. **Index terms**: 0320, 0394, 3354, 3360.

1. Introduction

Much of our planets precipitation originates as snow far above the surface of the Earth. Indeed, understanding the hydrological cycle requires a good working knowledge of the production of the ice particles that contribute to snow and rain under a variety of meteorological conditions. As a consequence of our knowledge of the physics of precipitation formation, rain from melting snow is indicated to be the dominant process in temperate zones, and also likely plays an important role in deep convective activity

worldwide. Although the microphysical processes describing the transition of snowflakes to raindrops are by now well understood, the corresponding effects on the propagation of laser light and microwaves would appear to require more research. Now that precipitating clouds are coming under scrutiny from Earth-orbiting radar systems, improving our understanding of the scattering and attenuation of microwaves in the melting layer is particularly warranted [*Simpson et al*., 1996; *Stephens et al*., 2003].

The most widely recognized remote sensing feature observed during the melting of snowflakes is the radar bright band. Named after the appearance of the narrow layer of strong signals on the oscilloscope displays of World War II vintage radars, it was not long before the main causes of the bright band were identified [for a review see *Battan*, 1973]. Because of the differences in the dielectric constants between water and ice particles, ice produces much weaker backscattering and attenuation in the Rayleigh regime, such that radar returns in the rain are strongly enhanced despite the larger sizes of the low-density (ice plus air mixture) snowflakes [*Meneghini and Liao*, 2000] and the fact that the concentration of raindrops declines significantly because their fallspeeds are much greater than the snowflakes they are derived from. A major factor contributing to the radar bright band is a consequence of the manner in which snowflakes melt—the ice surfaces become coated with liquid to a sufficient depth to scatter essentially like equivalent-sized water particles. These wet snowflakes are nonspherical and still relatively large, which generates strong microwave backscattering. Other factors that may come into play involve the aggregation/coalescence or breakup of snowflakes and raindrops, which, because of the diameter-to-the-sixth D^6 power law of Rayleigh scattering, can have noticeable effects on radar signals. At millimeter wavelengths a bright band effect is typically absent, and a radar dark band has even been reported for W-band radars near the expected bright band position [*Lhermitte*, 1988]. There is an analog of the bright band with lidar, but the lidar bright band owes its existence to the strong backscattering coupled with the overwhelming (i.e., exponential) attenuation rate in the snowfall surrounding the freezing level, which can create a feature resembling a bright band on an oscilloscope display [*Sassen*, 1977a].

The lidar dark band is a recently recognized curiosity of remote-sensing melting layer features. Although long serendipitously captured in lidar returns from precipitation,

its meaning and significance were concealed essentially because of a lack of prolonged data collection in rainfall: lidar systems needed to be shielded from precipitation, and other (optically less-dense) targets were favored. It was not until relatively recently that *Sassen and Chen* [1995] comprehensively studied this phenomenon and gave it a name. More recent observations have been reported in *Demoz et al.* [2000] and *Roy and Bissonnette* [2001]. The term lidar dark band, in obvious contrast to the radar bright band, delineates its quintessential property. It is a backscatter intensity minimum that occurs in the melting layer, apparently not far in height from the location of the radar bright band. Based on an analysis of coordinated aircraft, polarization lidar, and W-band (0.32 cm) Doppler radar measurements, it was concluded by *Sassen and Chen* [1995] that this "remarkably narrow and consistent feature" corresponded to a stage of snowflake melting that produced "inhomogeneous ice-containing raindrops formed by the structural collapse of severely melted snowflakes". According to laboratory studies of melting drops, the presence of an ice mass within a drop suppresses a major backscattering mechanism in spheres—the axial ray bundle reflected off the far face of the drop [*Sassen*, 1977b]. The increase in backscattering aloft of the dark band center could be attributed to the steady increase in low-density snowflake cross sectional areas in going from wet to dry snowflakes [*Sassen*, 1977a].

Unfortunately, it has yet to be determined how representative the *Sassen and Chen* [1995] findings are, particularly with regard to the melting layer temperature structure, the precipitation rate and mechanism, and how measurements at other radar wavelengths would have compared. The same can be said of the representativeness of the available W-band radar dark band case studies. These issues are addressed in the current study based on a unique ensemble of remote sensors.

2. The Dataset

The Cirrus Regional Study of Tropical Anvils and Cirrus Layers-Florida Area Cirrus Experiment (CRYSTAL-FACE) field campaign, which was carried out during July 2002 in the southern Florida region, was designed to research subtropical thunderstorms and the cirrus clouds derived from their anvils. In addition to six project aircraft, three surface sites were equipped with various ensembles of remote sensing systems to obtain

more continuous atmospheric observations and serve as hubs for the aircraft operations. The eastern site at the Kendall-Tamiami Executive Airport (~25 km southwest of Miami) was uniquely equipped with three Doppler radars and a radiation measurement suite that included a near-continuously operated eye-safe lidar (see Table 1 for remote sensor specifications). Data were also collected by a Joss-Waldvogel disdrometer located at this site to obtain high (1-min) resolution rainfall rate measurements. It should be noted, however, that surface rain measurements can differ greatly from conditions aloft in the melting region (~3.5 to 4.5 km above sea level in this case) because of temporal variations in the showers. Figure 1 shows an aerial photograph of the major instruments **as** deployed at the field site.

The micropulse (0.523 μm) lidar [MPL, *Spinhirne*, 1993] is a compact, eye-safe device, which is being increasingly utilized worldwide at ground-based observing sites for unattended cloud and aerosol observations. Eye-safety is achieved by using a rapidly-pulsed (2.5 KHz), low-powered (1.0 W) laser source expanded through a transmit/receive Cassegrain telescope. This feature allows the instrument to be operated full-time in autonomous fashion. (At CRYSTAL-FACE, however, data collection was typically suspended around solar noon- the lidar siesta time of the tropics- due to the excessive ambient solar background that adversely affected the photon-counting detector.) *Campbell et al.* [2002] have recently summarized the relevant MPL data processing techniques.

The three participating zenith-pointing Doppler radar systems represent a unique combination of millimeter-wave to microwave sensors (see Table 1). Atmospheric probing at the shortest 0.32-**c**m (94 GHz frequency) wavelength of W-band radars is sensitive to relatively small cloud droplets and ice crystals, although pulse attenuation in rain and melting snow can have noticeable effects on the returned signals. The University of Miami Doppler cloud radar UMDCR [*Albrecht et al*., 1999] is a single-antenna version of the radar developed during the early 1980's [*Lhermitte*, 1988]. The lightweight UMDCR uses a high pulse repetition frequency that yields a Doppler velocity window of ± 8 ms^{-1} at high spatial and temporal resolutions (typically 30 m in height by 1-s). With an antenna beamwidth of 0.24°, the radar horizontal sample size is about 20-m at 5 km. Real time signal processing is done in with a 14-bit Gage A/D board and PC based CPU. High

FFT-point Doppler spectra are provided by a real-time FFT algorithm (256, 512 or 1024 FFT points) at all range gates sampled by the processor. The high point FFT gives excellent Doppler spectra resolution.

At the somewhat longer 0.86-cm wavelength (34.86 GHz frequency) K_a-band wavelength, the NOAA millimeter cloud radar [MMCR, *Moran et al*., 1998] shares many of the capabilities of the W-band radar, but with reduced attenuation effects. The MMCR provides continuous profiles of the equivalent radar reflectivity factor Z_e ($mm^6\ m^{-3}$) and the Doppler spectrum through clouds and precipitation with approximately 10-s temporal and 45-90 m vertical resolution, using 128 FFT points. In spite of a low peak transmitted power of 100 W, the MMCR achieves high sensitivity using a large antenna, long sampling times, and pulse compression techniques.

In contrast to the millimeter-wave radars, the NOAA 10.6-cm (2.835 GHz frequency) S-band radar cannot generally observe the particles suspended in a cloud, but rather observes the larger particles that are precipitating out of the cloud. Such radars are *traditional* in the sense that pulse attenuation is rarely significant and the returned radar signals can be treated relatively simply with Rayleigh theory. This vertically pointing profiler [*Ecklund et al*., 1999] uses a 3-m parabolic dish antenna and a peak power of 500 W to observe the precipitating particles while they advect overhead. This unit operated with a 10-s temporal and a 60-m vertical resolution and alternated between an un-coded and a 10-bit coded pulse compression modes. The wavelength and sensitivity of this radar limits this radar to resolve particles that are essentially large enough to have a noticeable terminal fallspeed.

During the early part of the campaign of interest here, a broadening area of low pressure developed in the south-central Gulf of Mexico, yielding easterly to southeasterly low-level flow over the research area. In contrast to the usual strong diurnal convective activity expected during mid-summer months [*Michaels*, 1985], rainfall at this time was often more continuous in nature. While not inhibiting strong convective cell development, more stratiform rainfall events were also encountered. Such conditions are more amenable for observing radar/lidar melting layer phenomena than in strong thunderstorms, with their intense vertical motions and highly variable precipitation conditions.

3. Data and Analysis

Prior to showing examples from the multiple remote sensor dataset, it is useful to overview the scattering conditions to be expected at each wavelength in the melting layer, where various Rayleigh and non-Rayleigh effects will be manifested. Lidar scattering can be described by the principles of geometric optics, where the exact shape and cross-sectional area of the ice, mixed-phase, and water particles govern the backscattering behavior, and the attenuation of the laser pulse will generally be significant. For S-band radar, it can be assumed that Rayleigh scattering dominates under these conditions, such that hydrometeor scattering can be treated with spherical and spheroidal dipole particle models, and is therefore governed by the D^6 power law and the particle refractive index (i.e., phase), while attenuation is unimportant. This corresponds to the traditional radar bright band scenario. However, at the millimeter W- and K-band radar wavelengths (λ), a mixture of Rayleigh and non-Rayleigh scattering effects will come into play. For example, although the size parameter ($\chi = \pi D/\lambda$) for a 5-mm diameter raindrop is 0.15 at λ = 10.6 cm, which lies within the upper limit of $\chi \approx 0.3$ for Rayleigh (spherical) particles [*Kerker*, 1969], the $\chi \approx 2.0$ and 5.0 for the 0.86- and 0.32-cm wavelengths, respectively, violate the Rayleigh approximation to an increasing degree. Thus, melting layer observations at millimeter wavelengths present great challenges to interpret in comparison to the relative simplicity of traditional radar Rayleigh theory.

A four remote-sensor example of the appearance of the various melting layer phenomena over a 5-h period on 8 July is given in the height versus time backscattering displays in Figure 2, where sensor wavelength decreases from top to bottom. Note that a color radar reflectivity scale in dBZ (10 times log $mm^6\ m^{-3}$) is given to the right of each radar display, and that the range-normalized attenuated lidar backscattering (in arbitrary units) is also based on a logarithmic scale. Over this period, rainshowers of various intensity occurred (see bottom panel for surface disdrometer rainfall rate data). The S-band radar display at top shows a consistent radar bright band centered at ~4.3 km height above mean sea level (MSL), whose intensity tends to vary with the rainfall rate. The K-band radar display sometimes indicates a relatively weak bright band at a similar height, under weak precipitation conditions. Although no evidence for a bright band is apparent

in the W-band radar display, a radar dark band is sometimes indicated by a decline in radar signals at ~4.5 km, where dBZ are increasing at the other wavelengths (see below).

The lidar display is quite dissimilar because of the dominating effects of optical attenuation by hydrometeors, especially in the occasional water clouds below 1.0 km and from ~3.0 - 4.0 km MSL. Lidar dark bands are easily seen centered just above 4.0 km from around 1350-1440 and 1615-1720 UTC, which corresponds to periods when the lidar was able to penetrate high enough to sample the snow causing the rain. Note that the rapid signal decrease with height in the snow aloft is due to overwhelming attenuation, which produces a virtual bright band at ~4.5 km, as verified by the radar data indicating much higher cloud top heights. It is also interesting to note the differences in the cloud top heights sensed by the S- and W-band radars, which reflect the effects caused by variable wavelength-dependent attenuation rates versus the λ^{-4} sensitivity to particle size that favors ice cloud detection by millimeter-wave radars. Note that although the K-band radar in this case had a faulty pre-amplifier, which reduced signal levels by ~20 dBZ, the ice cloud top heights are higher than at 10.6 cm in the absence of strong rainfall-induced attenuation. Particularly near the end of the period, the W-band radar senses more of the non-precipitating clouds present due to the λ^{-4} Rayleigh law. These melting layer features are examined in greater detail below for these and an additional case study.

Given in Figures 3-5 are comparisons of profiles from the 10-min average MPL and Doppler radar datasets for three periods on the indicated days showing obvious lidar dark bands. The closest Miami radiosonde temperature profiles are given at right (the location of 0°C is highlighted), but it should be acknowledged that precipitation process can significantly alter the local atmospheric structure and make routine (12-hourly) sounding data unrepresentative [*Steward et al*., 1984]. (For example, note the presence of the isothermal layer in Figure 4 likely caused by the local cooling effect of melting snowflakes.) The data quantities are attenuated returned power for lidar (in arbitrary units), and Z_e and mean Doppler velocity V for the three radars. Note that the radar dBZ scale is valid in each case for the S-band data, with the W- and K-band profiles often adjusted to compress the dynamic range of the total signals and facilitate the data intercomparison (see figure caption). As indicated in Figure 2, millimeter-wave radar

returns are often much weaker because of non-Rayleigh scattering effects (i.e., the largest particles backscatter according to D^2 rather than D^6), and their radar pulse attenuation rates can be significant in the melting zone. Thus, we are more interested in the relative variations in the radar signals than their absolute magnitudes. The profiles bracket the melting layer from 2.0 to 7.0 km MSL, and shown in each case for reference as the horizontal green line is the height of the maximum S-band signal in the bright band.

Figure 3 provides a case from the morning of 8 July corresponding to a moderate rain shower (see Figure 2): the10-min average rainfall rate measured at the ground by the disdrometer was 1.52 mm h^{-1}. Strong optical attenuation is apparent in the rain and snow, which contributes to a relatively narrow lidar bright band centered near the 0°C isotherm. The lidar dark band is broad in this case with two signal minima, and this structure was persistent with time. The radar profiles show large Z_e increases from the top to the bottom of the melting layer, but the details differ significantly. A radar dark band is apparent at the top of the melting zone in the W-band data, while a bright band occurs in the S-band radar data at a lower height. The absence of W- and K-band bright bands indicates that Rayleigh scattering conditions in the melting snow were violated at these wavelengths. The Doppler mean velocities also show a steady increase in the melting layer. However, although the V are similar at ~1.5 m s^{-1} in the snowfall, the W-band fallspeeds abruptly stop increasing at ~4.5 m s^{-1}, also due to non-Rayleigh effects. That is, the K- and S-band radar Doppler V data are weighted toward the largest, fastest-falling raindrops, which are too large at the 0.32-cm wavelength to behave as Rayleigh scatterers. The uncommon occurrence of the dual minima in the lidar dark band is probably a result of the presence of a mixture of ice particle fallstreaks with different size or type characteristics: note the corresponding broad S-band radar bright band and the kink in the W-band radar V profile in the lower melting layer.

The two cases in Figures 4 and 5 are from light intensity rain showers (0.07 and 0.09 mm h^{-1} at the ground, respectively), under which conditions the lidar signals are obtained from greater heights above the strongly-peaked lidar bright bands owing to the smaller overall attenuation rates. The increasing lidar and radar signals in the rain with height above the surface indicate that the rainshowers were in the process of descending, or that raindrop evaporation in the light rain was occurring. The lidar dark bands in each

case are rather symmetrical and centered ~100 m below peaks in the S-band radar bright bands. In Figure 4, from the afternoon of 8 July (see Figure 2), a K-band radar bright band is clearly indicated, with a peak slightly below the S-band radar bright band center. Although certainly not a bright band, a barely discernable W-band radar signal peak also occurs at this height. Furthermore, all three Doppler radar V profiles are in reasonable agreement, peaking at ~3.5 m s^{-1}. In other words, the particle sizes in the very light rain in this case did not significantly exceed the Rayleigh limit, and the disdrometer data show that few drops exceeded 1.0 mm diameter. It is also interesting that the K-band bright band signal maximum occurs between the heights of the 10.6-cm radar bright band peak and lidar dark band center, but whether this is a regular feature can not be determined from our sample generally containing larger rainfall rates.

As in Figure 3, the data from 11 July (Figure 5) again show wavelength-dependent Doppler velocity differences and the absence of radar bright bands in both the W- and K-bands. In other words, the absence of a K-band radar bright band indicates that the larger melting, *nonspherical* particles violated the Rayleigh scattering assumption, unlike the raindrops derived from them**.** A relatively weak W-band radar dark band is suggested. The lack of radar reflectivity changes with height in the snowfall aloft in this last case indicates that ice particle aggregation was not important above the melting layer, in comparison to the small Z_e increases seen in the other two cases. As pointed out by *Battan* [personal communication, 1978], any radar bright band theory that relies on processes such as particle aggregation or breakup is not likely to succeed universally.

4. Discussion

The interrelationships between the various optical and microwave melting layer features illustrated by the characteristic profiles in Figures 3-5 lead us to the conceptual wavelength-dependent model given in Figure 6. Here we use basic hydrometeor models to help explain the backscattering phenomena as low-density snowflakes (i.e., dendritic ice crystal aggregates) transit into homogeneous near-spherical raindrops [*Mitra et al*., 1990]. Although we show the position of the 0°C isotherm for reference, the temperature gradient in the melting layer may be highly variable due to evaporative cooling and other factors, so we choose not to provide a vertical temperature or height scale. It should also

be kept in mind that the exact nature of the ice particles undergoing the phase change, including their density, size distribution, and amount of riming, will affect the backscattering and velocity outcomes in the melting layer.

At left in Figure 6 is schematically illustrated the hydrometer type, starting at top with a dry snowflake, two melting snowflakes in which water coatings are accumulating on the ice crystal branches and inter-branch cavities of the shrinking particles, an irregular water-enclosed severely melted snowflake, a near-spherical mixed-phase drop, a drop with most of the ice melted, and finally a homogeneous raindrop. The relative size of the particles is based roughly on a 10:1 ice to water particle density ratio. These images are more or less what are actually sensed by lidar, where backscattering responds to the exact details of particle shape and composition. In contrast, further to the right is a characterization of the radar cross sections that a S-band radar would sense, where simple particle models can be employed and the difference in particle phase (i.e., refractive index) is of significance to backscattering. Such Rayleigh-scattering particle models are apparently always violated by the larger particles present in rainshowers with W-band radars, such that a mixture of the optical and microwave models is in effect sensed. Accordingly, K-band radars with their intermediate wavelengths may sense conditions somewhere between the S- and W- bands, depending on the sizes of the hydrometeors in each case. In the remainder of the figure are idealized lidar backscattering (with the generic effects of attenuation on returned power above the dark band included as the dashed line), and W- and S-band Z_e and V profiles.

First, it should be noted that the strong optical attenuation from snowflakes in the vicinity of the freezing level, *depending on the precipitation rate,* helps to create a lidar bright band. In the absence of aggregation, radar reflectivities and mean fallspeeds are constant in this region. As the snowflakes progressively melt below the 0°C isotherm and shrink in size, the returned lidar power steadily decreases and the radar Z_e increases due to the increasing liquid water content. However, we hypothesize that a W-band radar dark band initially occurs high in the melting region because a water coating on the largest snowflakes should theoretically generate a decrease in backscattering in these non-Rayleigh particles [*Battan*, 1973]. The lidar signals reach a minimum at a stage of snowflake melting typically corresponding to a position just below the S-band radar

bright band and even closer to the signal plateau in W-band radar Z_e. This leads us to conclude that the reason the lidar signals start to increase is because the wet snowflakes have collapsed into mixed-phase raindrops that can now benefit from spherical particle backscattering mechanisms, namely surface-waves and the front-face axial reflection. (This collapse happens when the surface tension of the accumulating liquid overwhelms the structural strength of weakened crystal branches.) Thus, the traditional radar bright band peak corresponds to Rayleigh scattering in the highly irregular water-coated particles just prior to mixed-phase raindrop formation. The lidar signal increase below the dark band center is aided by the removal from the drops center of the embedded ice mass due to melting and/or internal drop circulations [*Pruppacher and Beard*, 1970], which allows the final spherical particle contribution, the paraxial reflection off the far drop face, to come into play [*Ro et al*., 1968].

The idealized vertical V profiles in Figure 6 reinforce these inferences, although at first glance the S-band data would seem to indicate otherwise. Such traditional Doppler radar data show that particle fallspeeds continue to increase to near the bottoms of the radar bright and lidar dark bands. However, this position is much lower than the usual positions of the W-band radar reflectivity plateaus, which must more accurately demarcate the mean position of the final snowflake to raindrop transition. The W-band Doppler V profiles in Figures 3 and 5, for example, show that V levels off at a higher relative position in the melting layer, which also tends to correspond to the millimeter-wave signal plateaus and the lidar dark band center, than that position at S-band. Thus, since the mean Doppler velocities in the Rayleigh domain are weighed according to the D^6 power law, microwave radar data are strongly biased toward the few largest particles, which have fallen the fastest and melted the least.

5. Conclusions

In this study we intended to examine the nature of the lidar dark band using coordinated Doppler radar measurements in the melting region at three wavelengths spanning the micro- to millimeter-wave regions (0.32- to 10.6-cm). Presumably, the radar backscattering features are better understood, and should therefore aid in explaining the lidar dark band. However, the microphysical/backscattering model that has resulted

differs from previous models in some respects in both the optical and microwave domains. Unfortunately, as unique as this dataset is, lidar and radar depolarization data, which would have provided further information on the state of the melting particles, are not available from the instruments deployed at the eastern CRYSTAL-FACE field site.

Prior to this study much of what was known of the lidar dark band was restricted to a single comprehensive case study that established its relation to W-band Doppler radar data and suggested a likely cause for this melting layer feature [*Sassen and Chen*, 1995]. Our results confirm that mixed phase particles are indeed involved in both the creation and destruction of the lidar dark band, with the initial laser signal increase resulting from the emergence of major spherical particle backscattering mechanisms immediately after the structural collapse of snowflakes, which is then followed by the melting of the embedded ice to finally disclose the drop center to backscattering. The presence and relative location of the triple-wavelength radar melting layer phenomena here has been crucial in this assessment. The previous lidar dark band model developed in *Sassen and Chen* [1995] involves the same basic scenario but over-emphasizes the contributions of the rear axial backscattering component. Although in laboratory experiments using frozen pendent drops the particles backscattered ~1.5 to 5.0 times more energy after the central ice mass floated to the top of the drop [*Sassen*, 1977b], lidar dark bands in the field can have more significant overall signal increases. The pendent particle shape and experimental set-up (using a horizontally incident laser beam) does not provide the best model for melting snowflakes studied by zenith lidar. In other words, the frozen drops in the laboratory started out displaying some spherical backscattering properties, which a melted snowflake would not display. Moreover, the extent that mixed-phase raindrop nonsphericity affects the lidar melting layer phenomena remains to be determined. Strong lidar backscattering anisotropy from aerodynamically distorted raindrops has recently been reported using a scanning lidar [*Roy and Bissonnette*, 2001].

Comparison of the triple-radar returns in the bright band region reveals significant wavelength-dependent Z_e differences, as well as differences in the basic Doppler signatures. Because the Doppler V from the three radars are weighted toward different portions of the particle size distribution, the positions of the snowflake-to-raindrop transition (i.e., the snowflake structural collapse) appear to diverge as a consequence of

the violation of Rayleigh theory. The W-band radar measurements consistently failed to detect the strong backscatter enhancement that we refer to as the radar bright band, only a gradual Z_e increase due to the refractive index consequences of the phase change. K-band radar bright bands occur under light rainfall conditions, presumably due to the dielectric constant effect in relatively small (i.e., Rayleigh-scattering) wet snowflakes. The W-band radar V profiles, least affected by D^6 sampling effects, support the conclusion that the traditional radar bright band occurs immediately above the region that the severely melted snowflakes collapse into raindrops. In other words, although a water coating starts accumulating on the ice crystals high in the melting layer to begin increasing Z_e, it is not until a later stage when the melt water collects together within the particle by capillary action that the peak reflectivities are approached with microwaves. The subsequent collapse of these decidedly nonspherical mixed-phase particles into smaller near-spherical drops considerably reduces backscattering with a zenith radar.

As noted first by *Lhermitte* [1988], W-band radar Z_e often decrease in the upper melting region in another sort of dark band. This radar dark band was attributed to a Mie backscattering effect in which the mean ice particle size increased enough, perhaps from riming growth just above the 0°C level, to expose the first backscattering minimum in the Mie scattering function. (This corresponds to a ~1.0 to 1.6 mm particle diameter increase for W-band radar.) However, problems with this explanation caused by the widths of the particle size distribution and other factors were recognized in *Lhermitte* [2002], and the possibility that unrepresentative temperature soundings influenced this model should be considered. We also attribute the radar dark band to non-Rayleigh effects, but not to the direct Mie effect suggested by *Lhermitte*. In particular, while a water-coated snowflake displays increased backscattering in the Rayleigh regime, the opposite is true for larger particles due to the effects of the different refractive indices of water and ice. We can refer to this as the melting hail analogy, which causes non-Rayleigh ($\chi >\sim 2$, or $D >\sim$ 2mm at λ=0.32 cm) ice spheres to backscatter less energy when water-coated than when dry [*Battan*, 1973]. Although the concentric water/ice sphere model is not the best representation for melting snowflakes, it should generally pertain to this feature of the melting process. Lower in the melting layer, we presume that the shrunken melting snowflakes behave more like Rayleigh scatterers.

We emphasize, however, that the exact interrelationships between the various lidar and radar melting layer features will depend crucially on the precipitation rate, as well as the size distribution and type of ice particles about to undergo the phase change. Ice particle density and amount of riming will control the particle fallspeeds, and their melting rates. Thus, as indicated here, the details of the bright/dark phenomena can vary noticeably from case to case.

It is interesting that field research is still disclosing new aspects of the effects of melting layer microphysics on lidar and radar returns. As stated by *Lhermitte* [2002], "Even after fifty years of melting layer observations and studies in various parts of the world, we are still in need of detailed radar observations of reflectivity and Doppler velocity…using vertically pointing radars working at different wavelengths from 10 cm to a very short millimeter wave (3.2 mm)". The research reported here represents a step in this direction, which also fortunately incorporated the special information from the vastly different scattering conditions encountered at the 0.523 μm lidar wavelength.

Acknowledgments. This research was supported by NASA grants NAG5-11503, NAG5-13418, and agreement W-10041 from the CRYSTAL-FACE program, and NASA grant NAG5-9753 from the TRMM program.

Addresses:

Kenneth Sassen, 903 Koyukuk Drive, Geophysical Institute, University of Alaska Fairbanks, Fairbanks, AK 99775. email: ksassen@gi.alaska.edu

James R. Campbell, Science Systems and Application, Inc., c/o Code 912, NASA GSFC, Greenbelt, MD 20771. email: campbell@virl.gsfc.nasa.gov

Pavlos Kollias, Rosenstiel School of Marine and Atmospheric Science, Division of Meteorology and Physical Oceanography, 4600 Rickenbacker Cswy, University of Miami, FL 33149. email: pkollias@rsmas.miami.edu

Matthew Shupe, R/ET6, 325 Broadway, Boulder, CO 80305. email: Matthew.Shupe@noaa.gov

Christopher Williams, NOAA Aeronomy Labatory, 325 Broadway Boulder, CO 80305. email: cwilliams@al.noaa.gov

Jiang Zhu, 903 Koyukuk Drive, Geophysical Institute, University of Alaska Fairbanks, Fairbanks, AK 99775. email: jzhu@gi.alaska.edu

References

Albrecht, B., P. Kollias, R. Lhermitte and R. Peters, Observations of tropical cloud systems with a MM-wavelength Doppler radar: An Overview. Preprints, 29th International Conference on Radar Meteorology. Montreal, Canada, 1999.

Battan, L. J., *Radar Observation of the Atmosphere*, Univ. Chicago Press, Chicago, 1973.

Campbell, J. R., D. L. Hlavka, E. J. Welton, C. J. Flynn, D. D. Turner, J. D. Spinhirne, V. S. Scott, and I. H. Hwang, Full-time, eye-safe cloud and aerosol lidar observation at Atmospheric Radiation Measurement Program Sites: Instruments and data processing, *J. Atmos. Oceanic Technol., 19*, 431-442, 2002.

Demoz, B., D. O'C. Starr, D. Whiteman, K. Evans, D. Hlavka, and R. Peravali, Raman lidar detection of cloud base, *Geophys. Res. Lett*., 27, 1899-2002, 2000.

Ecklund, W. L., C. R. Williams, P. E. Johnston and K. S. Gage, A 3 GHz profiler for precipitating cloud studies. *J. Atmos. and Oceanic Technol.*, **16**, 309-322, 1999.

Kerker, M., *The Scattering of Light and Other Electromagnetic Radiation*, Academic Press, New York, 1969.

Lhermitte, R., Observation of rain at vertical incidence with a 94 GHz Doppler radar: an insight on Mie scattering, *Geophys. Res. Lett.,* 15, 1125-1128, 1988.

Lhermitte, R., *Centimeter and Millimeter Wavelength Radars in Meteorology*, Lhermitte Productions, Miami, 2002.

Meneghini, R., and L. Liao, Effective dielectric constants of mixed-phase hydrometeors, *J. Atmos. Ocean. Tech*., 17, 628-640, 2000.

Michaels, P.J., Anomalous mid-atmospheric heights and persistent thunderstorm patterns over Florida, *J. Climate*, 5, 529-542, 1985.

Mitra, S. K., O. Vohl, M. Ahr, and H. R. Pruppacher, A wind tunnel and theoretical study of the melting behavior of atmospheric ice particles. VI: Experiment and theory for snow flakes, *J. Atmos. Sci*.,47, 584-591, 1990.

Moran, K. P., B. E. Martner, M. J. Post, R. A. Kropfli, D. C. Welsh, and K. B. Widener, An unattended cloud-profiling radar for use in climate research, *Bull. Amer. Meteor. Soc*., 79, 443-455, 1998.

Pruppacher, H. R., and K. Beard, A wind tunnel investigation of the internal circulation and shape of water drops falling at terminal velocity in air, *Quart. J. Meteor. Soc*., 96, 247-256, 1970.

Ro, P. S., T. S. Fahlen, and H. C. Bryant, Precision measurement of water droplet evaporation rates, *Appl. Opts*., 7, 883-890, 1968.

Roy, G., and L. R. Bissonnette, Strong dependence of rain-induced lidar depolarization on the illumination angle: experimental evidence and geometrical-optics interpretation, *Appl. Opt*., 40, 4770-4780, 2001.

Sassen, K., Lidar observations of high plains thunderstorm precipitation, *J. Atmos. Sci*., 34, 1444-1457, 1977a.

Sassen, K., Optical backscattering from near-spherical water, ice and mixed phase drops, *Appl. Opt*., 16, 1332-1341, 1977b.

Sassen, K., and T. Chen, The lidar dark band: An oddity of the radar bright band analogy, *Geophys. Res. Lett.,* 22, 3505-3508, 1995.

Simpson, J., C. Kummerow, W. K. Tao, and R. F. Adler, On the Tropical Rainfall Measuring Mission (TRMM), *Meteor. Atmos. Phys.*, 60, 19-36, 1996.

Spinhirne, J. D., Micro pulse lidar, *IEEE Trans. Geo. Rem. Sen*., 31, 48-55, 1993.

Stephens, G. L., D. G. Vane, R. Boain, G. G. Mace, K. Sassen, Z. Wang, A. Illingworth, E. O'Conner, W. B. Rossow, S. L. Durden, S. Miller, R. Austin, A. Benedetti, and C. Mitrescu, The CloudSat mission and the A-train: A new dimension of space-based observations of clouds and precipitation. *Bull. Amer. Meteor. Soc*., **83**, 1771-1790, 2003.

Steward, R. E., J. D. Marwitz, J. C. Pace, and R. E. Carbone, Characteristics through the melting layer of stratiform clouds, *J. Atmos. Sci*., 41, 3227-3237, 1984.

Figure Captions

Figure 1. Aerial photograph of the eastern CRYSTAL-FACE field site at the Kendall-Tamiami Executive Airport near Miami, where clockwise from the top right of the tarmac are the roof-mounted NOAA W-band Doppler radar, the NASA Surface Measurements for Atmospheric Radiative Transfer (SMART) van that held the MPL and several radiometers, the circular rain-guard enclosing the NOAA S-band radar dish, and the free-standing University of Miami W-band Doppler radar attached to its supporting van.

Figure 2. Comparison of returned laser energy and triple radar reflectivity factor Z_e height versus time displays over the 1300 to 1800 UTC period on 8 July 2002, during a series of rainshowers. Gaps in the data records are present for all but the S-band system. The bottom panel provides the surface rainfall rate measured by the disdrometer**.**

Figure 3. From left to right, 10-min average vertical profiles of relative returned laser power P(R) from the MPL, equivalent radar reflectivity factor Z_e (in dBZ) and mean Doppler velocity V for the three radars (see inserted color key), and temperature from the closest Miami (MIA) radiosonde, over the indicated time on 8 July 2002. The horizontal green line gives the height of the maximum S-band radar bright band signal. The range of radar reflectivities has been compressed by adding 22 dBZ and 5 dBZ to the W-band and K-band data, respectively. This signal manipulation is warranted in view of radar Z_e uncertainties caused by non-Rayleigh scattering effects, and also to some extent by radar calibration and sampling issues (see Table 1).

Figure 4. As in Figure 3, except that 8 dBZ was added to the W-band radar reflectivity factors.

Figure 5. As in Figure 3, except that 13 dBZ was added to the W-band radar reflectivity factors.

Figure 6. A schematic representation of the hydrometeor shapes responsible for the various lidar and radar bright and dark band features of the melting layer. In the left two panels are detailed models of melting dendritic snowflakes (i.e., from top to bottom) that visible-wavelength lidars would sense and the corresponding lidar

backscatter coefficients (β), with the effects of laser pulse attenuation shown by the dashed line. In the middle is a representation of the corresponding models that a S-band radar would sense. At right are idealized vertical profiles of radar Z_e and V for W- (dashed) and S-band radar. The relative position of the 0°C isotherm is shown for reference, and the horizontal dotted line corresponds to the lidar dark band signal minimum.

Table 1. Specifications of the micropulse lidar (MPL) and the three radars deployed at the eastern CRYSTAL-FACE field site. The differences exemplify the wavelength-dependent range of operational characteristics of modern remote sensors.

	MPL	W-band	K-band	S-band
Wavelength	0.523μm	0.32 cm	0.86 cm	10.6 cm
Peak Power (W)	1.0	1000	100	500
Maximum PRF (KHz)	2.5	10	7.7	8.0
Pulse Width	10 ns	200	0.3 μs	0.4 μs
Beamwidth	50 μrad	0.24°	0.3°	3.0°
Receiver Diameter (m)	0.2	0.9	1.8	3.0
Receiver Gain (dBZ)	--	58	165	--
Range Resolution (m)	75	30	45-90	60
Time Resolution (s)	60	60	9-35	10
Range Gates	800	512	184	244
Sensitivity @ 5.0 km	--	-37 dBZ	-28 dBZ	-6 dBZ
V Resolution (cm/s)	--	3.2	6.4	13.9

FIGURE 1

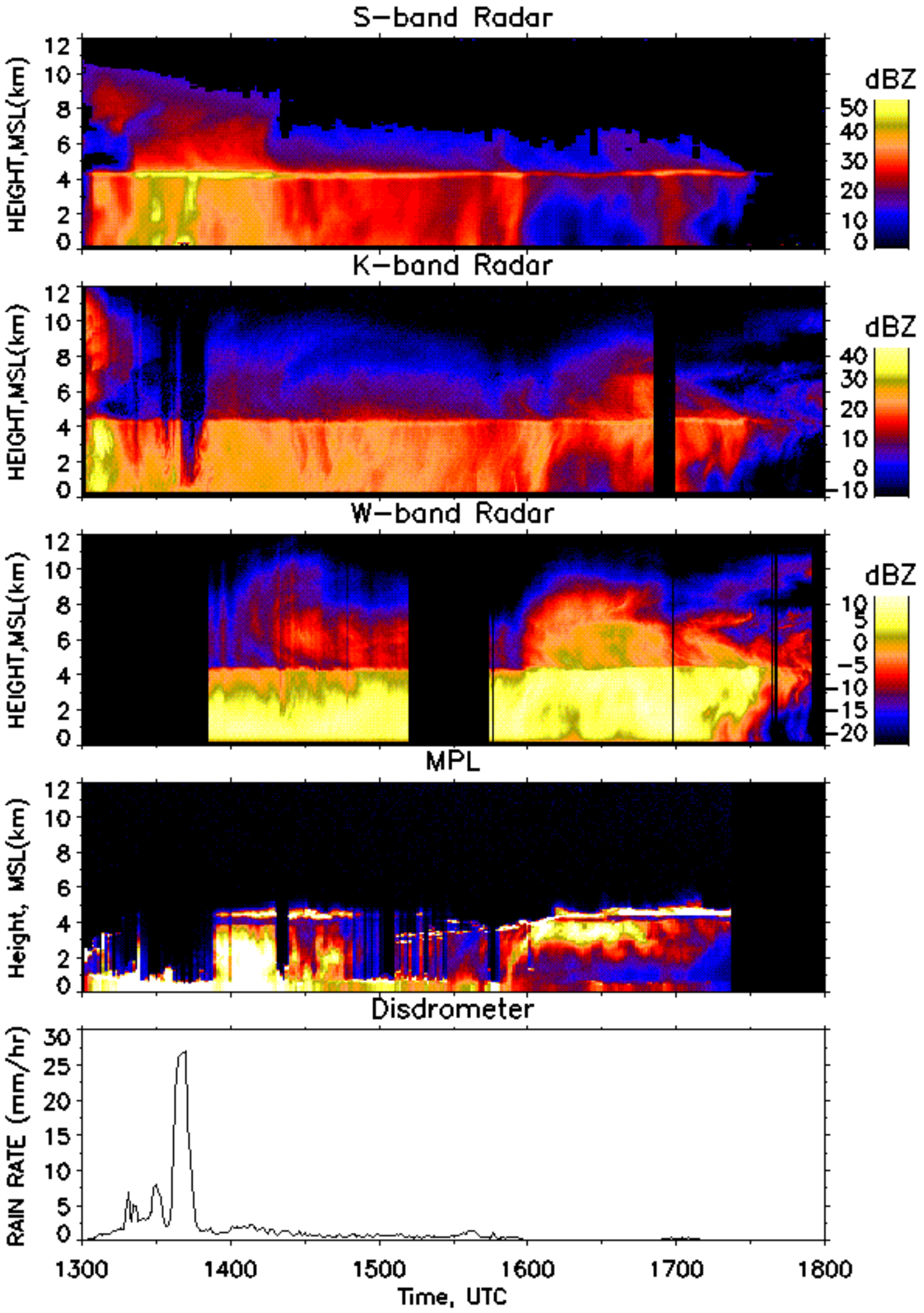
S-band Radar
HEIGHT,MSL(km)
dBZ
K-band Radar
HEIGHT,MSL(km)
dBZ
W-band Radar
HEIGHT,MSL(km)
dBZ
MPL
Height, MSL(km)
Disdrometer
RAIN RATE (mm/hr)
1300
1400
1500
1600
1700
1800
Time, UTC

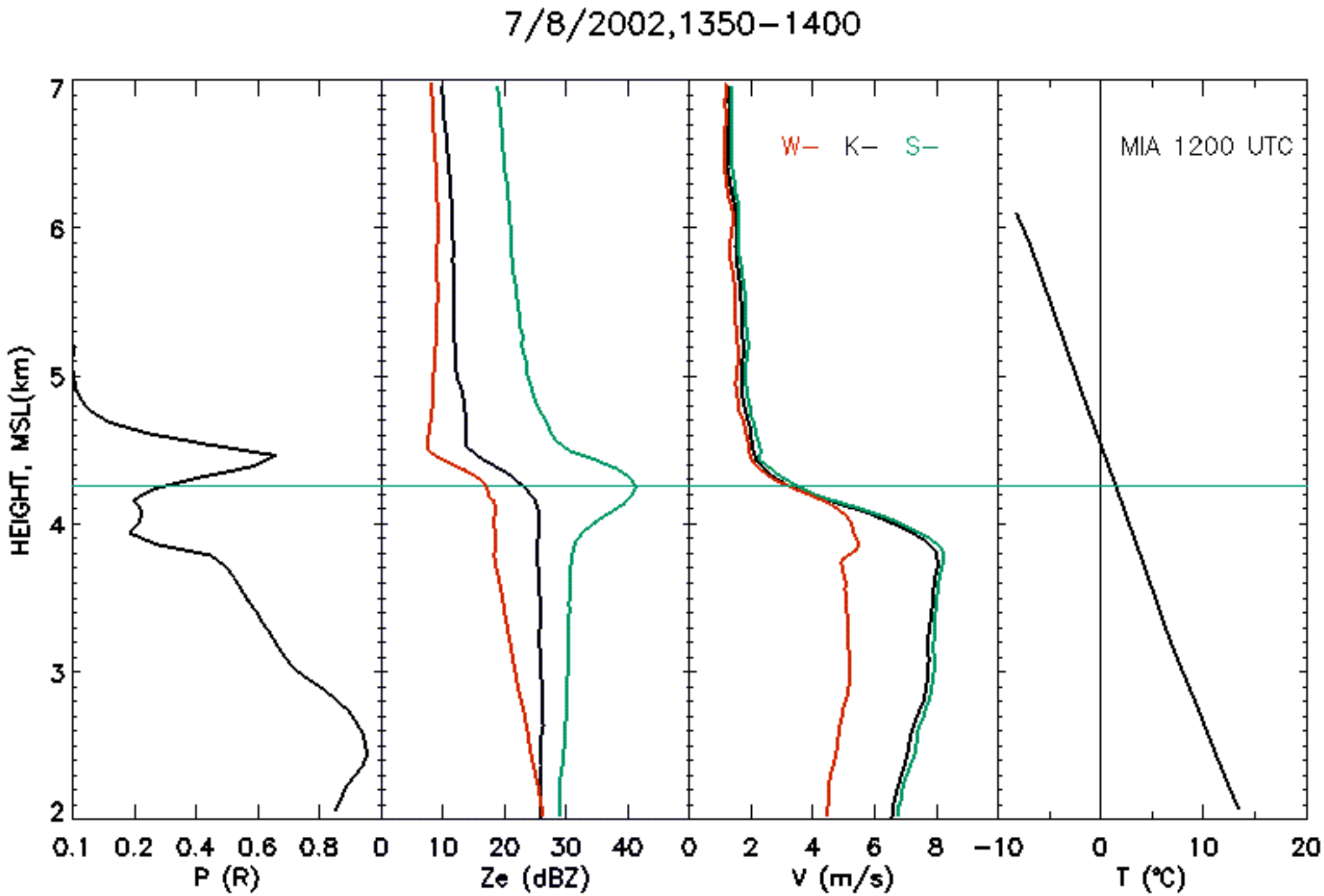
7/8/2002,1350–1400
HEIGHT, MSL(km)
7
6
5
4
3
2
0.1 0.2 0.4 0.6 0.8
P (R)
0 10 20 30 40
Ze (dBZ)
W– K– S–
0 2 4 6 8
V (m/s)
MIA 1200 UTC
–10 0 10 20
T (°C)

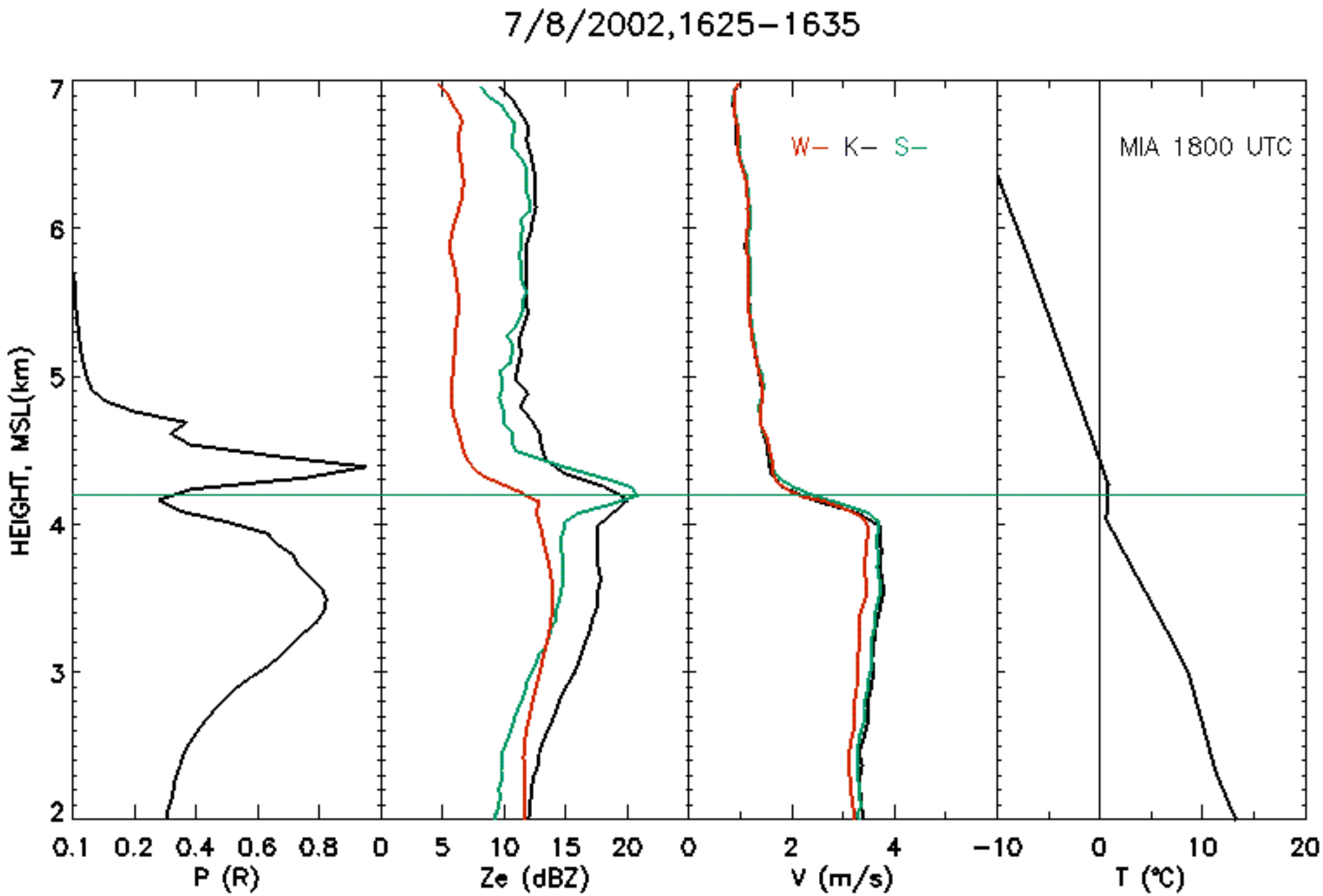
7/8/2002,1625–1635
HEIGHT, MSL(km)
7
6
5
4
3
2
0.1 0.2 0.4 0.6 0.8
P (R)
0 5 10 15 20
Ze (dBZ)
W– K– S–
0 2 4
V (m/s)
MIA 1800 UTC
–10 0 10 20
T (°C)

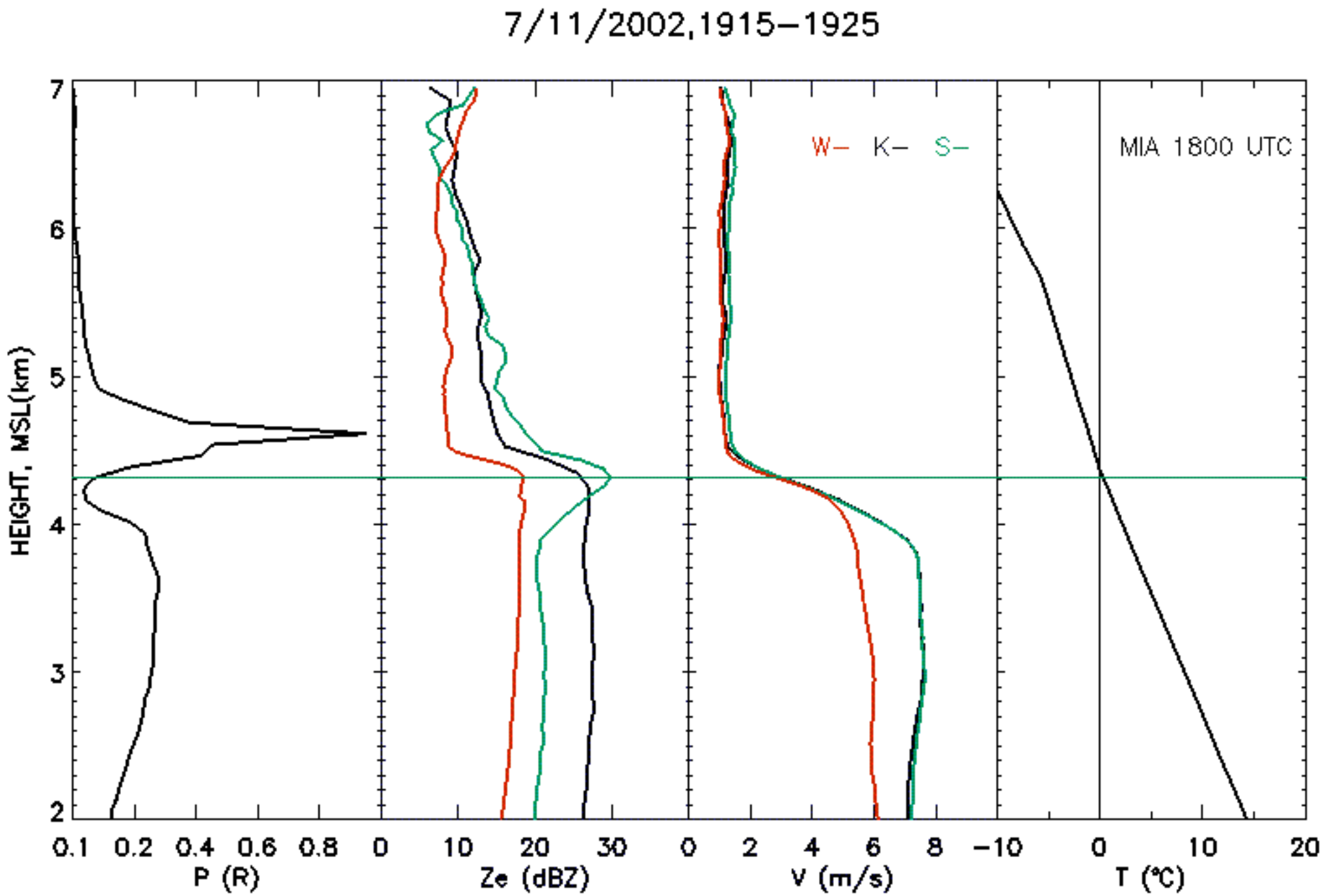
7/11/2002,1915–1925
HEIGHT, MSL(km)
7
6
5
4
3
2
0.1 0.2 0.4 0.6 0.8
P (R)
0 10 20 30
Ze (dBZ)
W– K– S–
0 2 4 6 8
V (m/s)
MIA 1800 UTC
–10 0 10 20
T (°C)

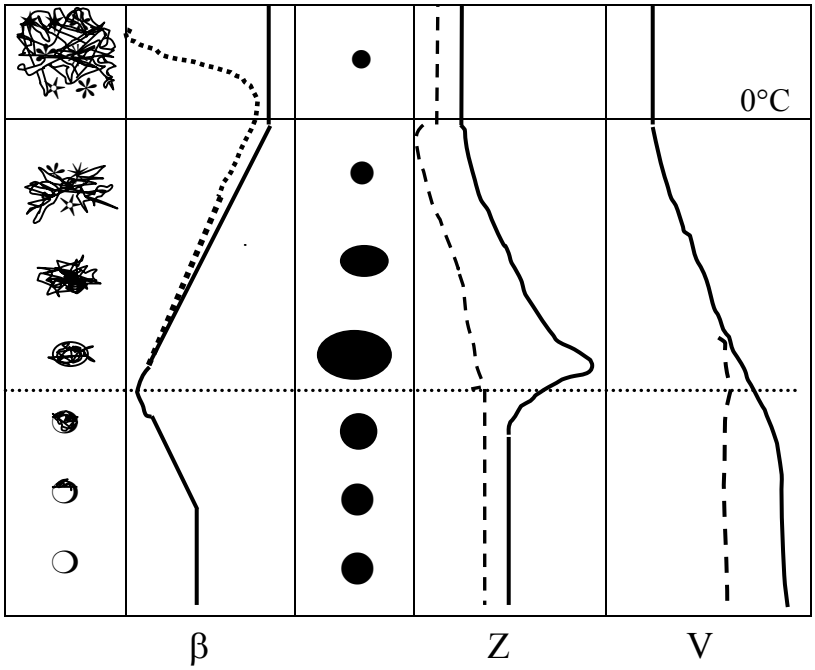
0°C
β
Z
V